

3-D Scattering Image Sparse Reconstruction via Radar Network

Le Kang, Ying Luo^{ID}, Member, IEEE, Qun Zhang^{ID}, Senior Member, IEEE, Xiao-Wen Liu^{ID}, and Bi-Shuai Liang

Abstract—Inverse synthetic aperture radar (ISAR) can only provide two-dimensional (2-D) images to represent the target's scattering projection on the corresponding imaging planes. However, as the echo of the target from different observation angles can be achieved simultaneously, the radar network can provide 3-D scattering information about the target. In this article, a novel 3-D scattering image reconstruction method is proposed based on the radar network and compressed sensing (CS). First, the general signal model and the reconstruction conditions of the radar network 3-D reconstruction are given. Then, the 3-D scattering distribution reconstruction model is built in a CS framework, which can reconstruct the positions and coefficients of scattering centers simultaneously. Moreover, the sparse structure with three layers in radar network 3-D reconstruction is defined and a fast 3-D reconstruction algorithm is proposed. To the end, the numerical simulations under noise scenarios and the principle prototype experiments on real data are shown to demonstrate the validity of the proposed method.

Index Terms—3-D image reconstruction, compressed sensing (CS), inverse synthetic aperture radar (ISAR) imaging, radar network.

I. INTRODUCTION

INVERSE synthetic aperture radar (ISAR), which obtains range resolution by wideband transmitted signal and azimuth resolution by coherent angle synthesis, can provide radar images of air-maneuvering targets and sea-surface targets. Since shape structure information of targets can be extracted from high-resolution radar images, ISAR is a typical technique used for target recognition and surveillance applications [1], [2]. As the two-dimensional (2-D) ISAR images are the mapping of the target on the imaging plane, only incomplete scattering information can be extracted from a 2-D ISAR image for a target [3]. As the imaging plane is determined by the flight line of the target and the radar line of sight (LOS), tremendous differences in the ISAR images

Manuscript received July 2, 2020; revised October 26, 2020; accepted November 10, 2020. This work was supported by the National Natural Science Foundation of China under Grant 61631019 and Grant 61971434. (Corresponding author: Ying Luo.)

Le Kang, Xiao-Wen Liu, and Bi-Shuai Liang are with the Institute of Information and Navigation, Air Force Engineering University, Xi'an 710077, China, and also with the Collaborative Innovation Center of Information Sensing and Understanding, Xi'an 710077, China.

Ying Luo and Qun Zhang are with the Key Laboratory for Information Science of Electromagnetic Waves (Ministry of Education), Fudan University, Shanghai 200433, China, also with the Institute of Information and Navigation, Air Force Engineering University, Xi'an 710077, China, and also with the Collaborative Innovation Center of Information Sensing and Understanding, Xi'an 710077, China (e-mail: luoying2002521@163.com).

Color versions of one or more figures in this article are available at <https://doi.org/10.1109/TGRS.2020.3039351>.

Digital Object Identifier 10.1109/TGRS.2020.3039351

of the same target would be caused by the differences in observing time and target attitude [4]. Moreover, the imaging result would be invalid when the target flies along the LOS because there is no relative rotation between the target and the radar [5]. To overcome these limitations, the high-resolution three-dimensional (3-D) imaging technique, which can extract more information and represent the 3-D target geometry, has been explored [6].

Recently, radar network constituted by multiple separated radars has attracted increasing attention owing to the low cost and high degree of freedom. At first, the researches about radar network focus on improving target detection rate and generating 3-D target track. Then, the optimum resource allocation of detection and tracking tasks is considered for multitarget [7], [8]. Since the wideband radar can obtain 2-D ISAR images independently, the related researches about imaging via radar network focus on the multitarget imaging task allocation rather than the imaging method [9]. As the echo of a target from different observation angles can be achieved by the radar network simultaneously, it can provide additional information about the target. Therefore, the radar network is a kind of potential system to provide the 3-D image for aerospace targets.

Nowadays, the 3-D imaging methods can mainly be categorized into three frames including multiple-input multiple-output (MIMO) ISAR [10], interferometric ISAR (InISAR) [11], and ISAR movie [12]. MIMO ISAR extends the synthetic aperture to two dimensions to provide the 3-D scattering distribution of the target, and it can achieve many advantages in motion compensation [13], real-time imaging [14], and super-resolution imaging [15] based on the freedom of centralized MIMO array antennas. After range compression and azimuth compression, the signal received by MIMO antennas can be regarded as multiple ISAR images. In MIMO ISAR, the multiple ISAR images must be coherent, and the 3-D resolution is obtained by coherent processing of the multiple ISAR images for different antennas, which is similar to the pulse compression. InISAR employs interferometric processing between multiple ISAR images generated by multiple receiving antennas to estimate the 3-D geometry [11], [16]–[22]. In InISAR, the 3-D coordinate of each pixel on the ISAR images are determined by the geometry of antennas and the interferometric phase [16], [17]. Different methods are proposed based on different antenna forms, e.g., dual-antennas [18], [19], L-shaped three antennas [20], and the corresponding problems including squint model and image registration have been studied [21], [22].

For InISAR methods, image registration is the prerequisite for interferometric processing. Interferometric processing is meaningful only if the pixels on different images for the same scatterer are registered. ISAR movie utilizes a sequence of ISAR images in time domain to generate 3-D geometry of a target [12], [23]–[25]. The locations of scatterers are determined essentially by the track on the image plane with the assumption that the scatterers can be correctly associated with frame to frame [12]. The 3-D geometry can be estimated with relatively high accuracy since the resolution depends on that of the ISAR images. In the multistatic ISAR movie, which is the combination of InISAR and ISAR movie, the track on the image plane is obtained by the interferometric phases between the multistatic observations [26].

What the abovementioned methods have in common is that the 3-D images are generated by utilizing the relations of the multiple ISAR images. Though multiple ISAR images can also be independently generated by the radar network, the failure cause of the above methods for radar network 3-D imaging is that the relations are different in different imaging systems. Specifically, fully coherent ISAR images are easy to achieve for a centralized MIMO system such as MIMO ISAR; however, the ISAR images are generally noncoherent for the radar network. In InISAR methods, the spatial coherence of the different ISAR images can be utilized by interferometric processing after image registration. For radar networks, however, the observation angles are significantly different, and it may cause significant differences in target attitude. In this case, the shape change may appear between different ISAR images, and it is almost impossible for image registration. After scatterer association in ISAR movie methods, the temporal coherence of different ISAR images can be utilized to determine the locations of scatterers. For radar networks, however, the scatterers are difficult to be associated accurately due to the anisotropy scattering for different observation angles.

To avoid the above problems in radar network, another relation of the multiple ISAR images, which is the coherence of the multiple ISAR images in the 3-D inverse-projective space, is utilized to reconstruct the 3-D target geometry [27] and estimate the target parameters [28] by 0–1 programming. In these Programming-based Radar Network (PRN) 3-D reconstruction methods, the locations of scatterers are determined by 0–1 programming with the assumption that the scattering coefficient is 0 or 1 for whether there is a scatterer or not. As a result, multiple binary images are utilized rather than the ISAR complex images in the other 3-D imaging methods. As the scatterer number is known, the 0–1 programming is to find the set of points with value 1 from all spatial points to minimize the difference between the ISAR images and the projection images, which is solved by genetic algorithm. However, since the searching space has a cubic increase rate with the resolution of the ISAR images, these methods cease to be efficient for the high-resolution cases. Besides, the scatterer number is generally unknown in the real case, and the information of the scattering coefficient is lost with the binarized assumption. Except for these problems, the reconstruction condition analysis and the

principle experiments should be given to further verify the feasibility of radar network 3-D reconstruction.

In this article, we propose a 3-D scattering image sparse reconstruction method. To hold the scattering coefficients, we utilize multiple ISAR images without binarization and the locations and coefficients are formed as a multiple measurement vector, which can be reconstructed together. To reduce the problem size, the layer sparse structure of radar network 3-D reconstruction is analyzed, and the upper bound of the scatterer number can be predicted before reconstruction. Moreover, we analyze the reconstruction conditions of radar network 3-D reconstruction, and the two principle prototype experiments on real data are shown to demonstrate the validity of the proposed method. The advantages of the proposed method are, therefore, five folds.

- 1) The proposed method is suitable for most situations only if the 2-D ISAR images of the target can be obtained.
- 2) The proposed method only requires the echo of several wideband radars, which is put almost no impact on the hardware requirement.
- 3) The proposed method can provide the 3-D scattering structure rather than a curved 2-D surface obtained by InISAR and has better antinoise performance.
- 4) The proposed method avoids the scatterer association in ISAR movie, so it is effective for real cases with a large number of scatterers and different observation angles.
- 5) The proposed method can reconstruct the scattering positions and scattering coefficients simultaneously.

This article is organized as follows. Section II formulates the signal model of radar network 3-D imaging, and Section III provides the reconstruction conditions. In Section IV, the radar network 3-D sparse reconstruction model is presented, and a fast 3-D reconstruction algorithm is described. Simulation experiments and the principle prototype experiments on real data are carried out in Section V to evaluate the proposed algorithm. Finally, the conclusion is summarized in Section VI.

II. RADAR NETWORK SIGNAL MODEL

The imaging geometry of the radar network is shown in Fig. 1, where several radars form a network and they can observe the target simultaneously and independently of different angles. The radar network is constituted by N_R available radars. The target is supposed to fly in the far field with velocity \mathbf{v} .

Suppose that the transmitted waveform of the radar- i in the radar network is $p_i(t_r)$, the received baseband echo signal can be expressed as follows:

$$s_i(t_r) = g_i(x, y)p_i(t_r - \tau) \cdot \exp(-j2\pi f_c \tau) \quad (1)$$

where $i \in \{1, 2, \dots, N_R\}$, t_r is the fast time, f_c is the carrier frequency, $g_i(x, y)$ denotes the scattering coefficient at (x, y) on the imaging plane for the radar- i , and τ is the time delay. Because the time delay τ changes with the slow time t_a , the echo signal of all the scattering centers can be rewritten as

$$\begin{aligned} s_i(t_r, t_a) = & \int \int_{x,y} g_i(x, y)p_i(t_r - \tau(t_a, x, y)) \\ & \cdot \exp(-j2\pi f_c \tau(t_a, x, y)) dx dy \end{aligned} \quad (2)$$

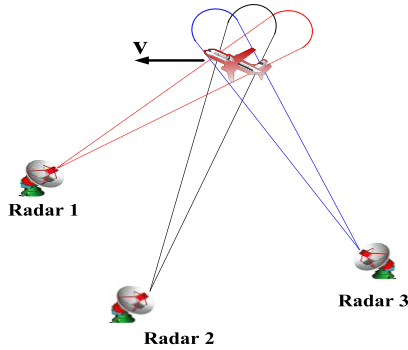


Fig. 1. Radar network geometry. The radars selected to form a network simultaneously and independently observe the target from different angles.

where $\tau(t_a, x, y)$ is the time delay for the scattering center at (x, y) when the slow time is t_a .

Suppose that the observation area is discretized by $n'_r = 1, 2, \dots, N'_r$ grids along the range direction and $n'_a = 1, 2, \dots, N'_a$ grids along the cross-range direction, the grid widths in the range and the cross-range directions are Δx and Δy , respectively. The scattering coefficients of $N'_r \times N'_a$ grid points can be expressed as

$$\mathbf{g}_i = [g_i(1, 1), \dots, g_i(n'_r, n'_a), \dots, g_i(N'_r, N'_a)] \quad (3)$$

where $g_i(n'_r, n'_a)$ is the simplified form of $g_i(n'_r \Delta x, n'_a \Delta y)$. Then, the echo signal is discrete in space domain

$$s_i(t_r, t_a) = \sum_{n'_r=1}^{N'_r} \sum_{n'_a=1}^{N'_a} g_i(n'_r, n'_a) \cdot p_i(t_r - \tau(t_a, n'_r, n'_a)) \times \exp(-j2\pi f_c \tau(t_a, n'_r, n'_a)) \quad (4)$$

where $\tau(t_a, n'_r, n'_a)$ is the time delay for the scattering center $(n'_r \Delta x, n'_a \Delta y)$ when the slow time is t_a .

Suppose that the sampling points of fast time and slow time are $n_r = 1, 2, \dots, N_r$ and $n_a = 1, 2, \dots, N_a$, the echo signal can be further expressed as

$$s_i(t_{r,n_r}, t_{a,n_a}) = \sum_{n'_r=1}^{N'_r} \sum_{n'_a=1}^{N'_a} g_i(n'_r, n'_a) \cdot a_i(n_r, n_a, n'_r, n'_a) \quad (5)$$

where t_{r,n_r} is the n_r th sampling point of fast time, t_{a,n_a} is the n_a th sampling point of slow time, $a_i(n_r, n_a, n'_r, n'_a)$ is equal to $p_i(t_{r,n_r} - \tau(t_{a,n_a}, n'_r, n'_a)) \exp(-j2\pi f_c \tau(t_{a,n_a}, n'_r, n'_a))$ for convenience, and $\tau(t_{a,n_a}, n'_r, n'_a)$ is the time delay for the scattering center at $(n'_r \Delta x, n'_a \Delta y)$ when the slow time is t_{a,n_a} .

To analyze the echo signal in a general model, the following equation is expressed as a matrix form (6) and (7), as shown at the bottom of the page, where \mathbf{s}_i and \mathbf{A}_i are the signal vector and the measurement matrix, respectively. Considering the environment noise, the echo signal can be expressed as

$$\mathbf{s}_i = \mathbf{A}_i \mathbf{g}_i + \boldsymbol{\eta} \quad (8)$$

where $\boldsymbol{\eta}$ is the noise vector.

Since the transmitting signal and geometry model are determined, \mathbf{s}_i and \mathbf{A}_i are known and the imaging problem is transformed into an estimation of the linear model. According to the estimation theory, the best estimator (also known as the minimum variance unbiased estimator) of \mathbf{g}_i can be expressed as $(\mathbf{A}_i^H \mathbf{D}^{-1} \mathbf{A}_i)^{-1} \mathbf{A}_i^H \mathbf{D}^{-1} \mathbf{s}_i$, where \mathbf{D} is the covariance matrix of noise $\boldsymbol{\eta}$. As another typical estimator, the least-square estimator of \mathbf{g}_i is $(\mathbf{A}_i^H \mathbf{A}_i)^{-1} \mathbf{A}_i^H \mathbf{s}_i$. In the white Gaussian noise environment, the least-square estimator is equal to the best estimator since $\mathbf{D} = \sigma^2 \mathbf{I}$, where \mathbf{I} denotes the identity matrix.

To obtain the best estimator, $(\mathbf{A}_i^H \mathbf{A}_i)^{-1} \mathbf{A}_i^H \mathbf{s}_i$, $\mathbf{A}_i^H \mathbf{A}_i$ should be invertible. In most cases, however, the grids are dense to provide more information about the target, which means that $N'_r N'_a \gg N_r N_a$ is satisfied. As the size of \mathbf{A}_i is $N_r N_a \times N'_r N'_a$, the rank of $\mathbf{A}_i^H \mathbf{A}_i$ is no more than $N_r N_a$. As the size of $\mathbf{A}_i^H \mathbf{A}_i$ is $N'_r N'_a \times N'_r N'_a$, $\mathbf{A}_i^H \mathbf{A}_i$ is not an invertible matrix.

To solve the above problem, the feasible way is to find the approximate estimator. For imaging algorithms based on matched filtering, e.g., the range-Doppler (RD) algorithm, \mathbf{g}_i is estimated as $\mathbf{A}_i^H \mathbf{s}_i$ by left-multiplying $\mathbf{A}_i^H \mathbf{A}_i$ with $(\mathbf{A}_i^H \mathbf{A}_i)^{-1} \mathbf{A}_i^H \mathbf{s}_i$ to avoid the ill-posed cases. For imaging algorithms based on regularization or compressed sensing (CS) theory, the estimation of \mathbf{g}_i is transferred to a well-posed problem by utilizing prior information of targets. The estimator of \mathbf{g}_i can be obtained by solving $\min_{\mathbf{g}_i} \|\mathbf{s}_i - \mathbf{A}_i \mathbf{g}_i\|_2^2 + J(\mathbf{g}_i)$, where $J(\cdot)$ is the penalty function based on prior information.

Since the radar network is constituted by multiple separated radars and the hardware of the radars may be different, different imaging methods may be used. Then, the imaging results for the target obtained by the radar network can be expressed as $\{\mathbf{g}_1, \mathbf{g}_2, \dots, \mathbf{g}_{N_R}\}$.

III. RADAR NETWORK 3-D RECONSTRUCTION CONDITIONS

The geometry model for radar network observation is shown in Fig. 2, where (O, X, Y, Z) denotes the local cartesian coordinate and O is the target center point determined by

$$\mathbf{s}_i = \mathbf{A}_i \mathbf{g}_i \quad (6)$$

$$\mathbf{s}_i = [s_i(t_{r,1}, t_{a,1}), \dots, s_i(t_{r,n_r}, t_{a,n_a}), \dots, s_i(t_{r,N_r}, t_{a,N_a})]^T$$

$$\mathbf{A}_i = \begin{bmatrix} a_i(1, 1, 1, 1) & \cdots & a_i(1, 1, n'_r, n'_a) & \cdots & a_i(1, 1, N'_r, N'_a) \\ \vdots & \ddots & \vdots & \ddots & \vdots \\ a_i(n_r, n_a, 1, 1) & \cdots & a_i(n_r, n_a, n'_r, n'_a) & \cdots & a_i(n_r, n_a, N'_r, N'_a) \\ \vdots & \ddots & \vdots & \ddots & \vdots \\ a_i(N_r, N_a, 1, 1) & \cdots & a_i(N_r, N_a, n'_r, n'_a) & \cdots & a_i(N_r, N_a, N'_r, N'_a) \end{bmatrix} \quad (7)$$

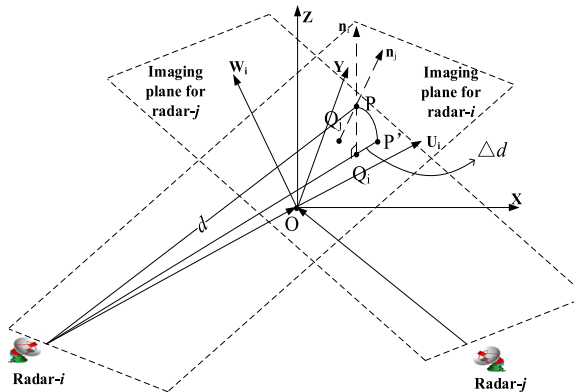


Fig. 2. Geometry of case-1. One point is projected on two imaging planes.

target tracking. For each radar, the imaging plane is determined by the flight line of the target and the radar LOS. (O, U_i, W_i) is the ISAR image coordinate system on the imaging plane for radar- i . n_i and n_j are the normal vectors of the imaging planes for radar- i and radar- j , respectively.

According to the ISAR imaging principle, a point in 3-D space will map to the point on the plane with the same distance to the radar. As shown in Fig. 2, L is the target size, and d is the range from the target to the radar, P' is the point mapped by point P along the circular arc, Q_i is the orthogonal projection of P , and d is the distance between P' and Q_i . In the far-field condition, since the distance $d \leq L^2/2d$ is normally less than the resolution of ISAR images, P' , the point mapped along the circle arc can be approximated to the orthogonal projection point Q_i . As a result, the mapping process and the inverse process are described by the following two axioms in the far-field approximation.

Axiom-1: For any radar, a given point in the space can be projected at one and only one point on the imaging plane along the normal vector, which can be expressed as

$$\forall i \in \{1, 2, \dots, N_R\}, \quad \forall P \in \mathbb{R}^3, \quad \exists! Q_i \in \mathbb{R}_i^2 \cap n_i \quad (9)$$

where \forall is the universal quantifier, \exists is the existential quantifier, $\exists!$ is the unique quantifier, P is a point in the space, \mathbb{R}^3 denotes the 3-D space, \mathbb{R}_i^2 denotes the imaging plane for radar- i , and \cap is the intersection operation.

Axiom-2: For a given point on an imaging plane, the inverse-projected point in the space may be located at anywhere on the normal vector of the imaging plane, which can be expressed as

$$\forall i \in \{1, 2, \dots, N_R\}, \quad \forall Q_i \in \mathbb{R}_i^2 \cap n_i, \quad \exists \tilde{P} \in \left\{ P_k \mid \overrightarrow{Q_i P_k} = k n_i, k \in \mathbb{R} \right\} \quad (10)$$

where \tilde{P} is the inverse-projected point of Q_i , P_k is the point on the normal vector n_i , and k is a variable in the real domain \mathbb{R} .

Case-1: Only one point P needs to be reconstructed, which is the simplest case.

If only the imaging plane for radar- i is unitized and the point P in the space is determined, the projection point on the i th imaging plane is known as $Q_i \in \mathbb{R}_i^2 \cap n_i$ according to (9). However, there are infinite possibilities for

the inverse-projected point \tilde{P} since k can be any real number in (10). So, one point P cannot be reconstructed correctly using only one imaging plane.

If only two imaging planes are unitized, the projection points on i th and j th imaging planes are known as $Q_i \in \mathbb{R}_i^2 \cap n_i$ and $Q_j \in \mathbb{R}_j^2 \cap n_j$ according to (9). Utilizing (10) for Q_i and Q_j , we can derive as

$$\begin{aligned} \forall i, j \in \{1, 2, \dots, N_R\}, \quad Q_i \in \mathbb{R}_i^2 \cap n_i, Q_j \in \mathbb{R}_j^2 \cap n_j \\ \Rightarrow \exists \tilde{P} \in \left\{ P_k \mid \overrightarrow{Q_i P_k} = k_i n_i, k_i \in \mathbb{R} \right\} \\ \cap \left\{ P_{k_j} \mid \overrightarrow{Q_j P_{k_j}} = k_j n_j, k_j \in \mathbb{R} \right\} \end{aligned} \quad (11)$$

where k_i and k_j are the two independent variables in the real domain. According to different relationships between n_i and n_j , (11) can be derived as

$$n_i = n_j \Rightarrow \exists \tilde{P} \in \left\{ P_k \mid \overrightarrow{Q_i P_k} = k n_i, k \in \mathbb{R} \right\} \quad (12)$$

$$n_i \neq n_j \Rightarrow \exists \tilde{P} \in n_i \cap n_j. \quad (13)$$

In (13), $P \in n_i \cap n_j$ if n_i and n_j intersect at one and only one point. Then, (13) can be divided into two cases as

$$n_i \cap n_j = \emptyset \Rightarrow \exists \tilde{P} \in \emptyset \Rightarrow \neg \exists \tilde{P} \quad (14)$$

$$n_i \cap n_j \neq \emptyset \Rightarrow \exists! \tilde{P} = P \quad (15)$$

where \emptyset is the null set and \neg is the negation sign. So, the reconstruction condition of Case-1 can be expressed as

$$\forall P \in \mathbb{R}^3, \quad \exists i, j \in \{1, 2, \dots, N_R\} \text{ s.t. } n_i \neq n_j, n_i \cap n_j \neq \emptyset. \quad (16)$$

Case-2: Two points P_1 and P_2 need to be reconstructed.

The ideal geometry of Case-2 is shown in Fig. 3. Q_{i1} and Q_{j1} are the projection points of P_1 on the imaging plane for radar- i and radar- j , respectively. Q_{i2} and Q_{j2} are the projections of P_2 on the imaging plane for radar- i and radar- j , respectively. Suppose that $|P_1 P_2| = l$, $|Q_{i1} Q_{i2}| = l_i$, and $|Q_{j1} Q_{j2}| = l_j$. If $l_i < \rho_{\text{ISAR}_i}$, where ρ_{ISAR_i} is the resolution of the ISAR image for radar- i , Q_{i1} and Q_{i2} are regarded as one point Q_i . If $l_j < \rho_{\text{ISAR}_j}$, Q_{j1} and Q_{j2} are also regarded as one point Q_j . So, the number of projected points maybe 2, 3, or 4 in Case-2.

If $l_i < \rho_{\text{ISAR}_i}$ and $l_j < \rho_{\text{ISAR}_j}$, the number of projected points is 2 and Case-2 is equal to Case-1. According to (12), (14), and (16), it is known that only 0, 1, and infinite points can be reconstructed from two projected points, respectively. So, the points P_1 and P_2 cannot be reconstructed correctly in this case.

If $l_i \geq \rho_{\text{ISAR}_i}$ and $l_j \geq \rho_{\text{ISAR}_j}$, the number of projected points is 4 and Case-2 can be divided into two independent Case-1 problems. As Case-1 can be correctly reconstructed based on conditions of (16), Case-2 can be correctly reconstructed to apply (16) for points P_1 and P_2 . So, the conditions of this case can be expressed as

$$\begin{aligned} \exists i, j \in \{1, 2, \dots, N_R\}, \quad n_i \neq n_j, n_i \cap n_j \neq \emptyset \\ \text{s.t. } l_j \geq \rho_{\text{ISAR}_j}, l_i \geq \rho_{\text{ISAR}_i}. \end{aligned} \quad (17)$$

If one of $l_i < \rho_{\text{ISAR}_i}$ and $l_j < \rho_{\text{ISAR}_j}$ is satisfied, the number of projected points is 3. Without loss of generality, $l_i \geq \rho_{\text{ISAR}_i}$

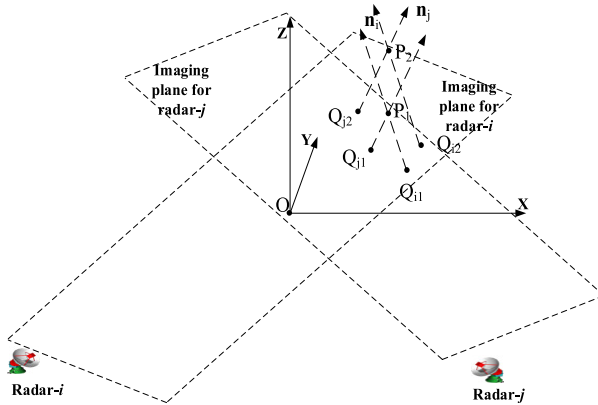


Fig. 3. Geometry of case-2. Two points are projected on two imaging planes.

is supposed to be satisfied and the projected points are Q_{i1} , Q_{i2} , and Q_j . Unlike (17), the reconstruction problem can be regarded as two related Case-1 problems. Since n_i through Q_{i1} and n_j through Q_j intersect at P_1 , (16) holds for P_1 . For the same reason, (16) holds for P_2 . So, the conditions of this case can be expressed as

$$\exists i \in \{1, 2, \dots, N_R\} \text{ s.t. } l_i \geq \rho_{\text{ISAR}_i}. \quad (18)$$

It can be found that (18) is contained in (17), so (17) is the better condition of Case-2.

Suppose the set of the scattering points on the target is denoted by \mathbf{C}_0 , $P_1, P_2 \in \mathbf{C}_0$, and $\overrightarrow{P_1 P_2} / |P_1 P_2| = n$. The vectors of the points Q_{i1} and Q_{i2} can be expressed as

$$\overrightarrow{OQ_{i1}} = \overrightarrow{OP_1} - \overrightarrow{Q_{i1}P_1} = \overrightarrow{OP_1} - (\overrightarrow{OP_1} \cdot n_i)n_i \quad (19)$$

$$\overrightarrow{OQ_{i2}} = \overrightarrow{OP_2} - \overrightarrow{Q_{i2}P_2} = \overrightarrow{OP_2} - (\overrightarrow{OP_2} \cdot n_i)n_i. \quad (20)$$

As $\overrightarrow{OP_2} = \overrightarrow{OP_1} + \overrightarrow{P_1 P_2}$, (26) can be rewritten as

$$\begin{aligned} \overrightarrow{OQ_{i2}} &= (\overrightarrow{OP_1} + \overrightarrow{P_1 P_2}) - ((\overrightarrow{OP_1} + \overrightarrow{P_1 P_2}) \cdot n_i)n_i \\ &= \overrightarrow{OQ_{i1}} + ln - l \cos \theta_i n_i \end{aligned} \quad (21)$$

where θ_i denotes the angle between n_i and n . The vector between Q_{i1} and Q_{i2} can be written as

$$\overrightarrow{Q_{i1}Q_{i2}} = \overrightarrow{OQ_{i2}} - \overrightarrow{OQ_{i1}} = ln - l \cos \theta_i n_i. \quad (22)$$

Then, the length between Q_{i1} and Q_{i2} is

$$\begin{aligned} l_i &= |l(n - \cos \theta_i n_i)| \\ &= l \cdot \sqrt{|n|^2 + |\cos \theta_i n_i|^2 - 2 \cos \theta_i n \cdot n_i} \\ &= l \cdot \sqrt{1 + \cos^2 \theta_i - 2 \cos^2 \theta_i} = l \sin \theta_i. \end{aligned} \quad (23)$$

So, (18) can be rewritten as

$$\exists i \in \{1, 2, \dots, N_R\}, |P_1 P_2| = ls.t. \sin \theta_i \geq \frac{\rho_{\text{ISAR}_i}}{l}. \quad (24)$$

Since $P_1, P_2 \in \mathbf{C}_0$ and they can be separated, $l \geq \rho_{\text{rec}}$ should be satisfied, where ρ_{rec} is the resolution of reconstruction results in space. If the angle θ_i satisfies the relationship as follows:

$$\sin \theta_i \geq \frac{\rho_{\text{ISAR}_i}}{\rho_{\text{rec}}} \quad (25)$$

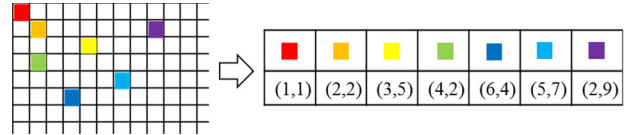


Fig. 4. Data representation. Any generally image can be transformed to an index image.

any two points on the target can be reconstructed correctly according to (24). If any two points can be reconstructed correctly, all the points can also be reconstructed correctly. So, the final reconstruction condition of radar network can be given as

$$\forall P_1, P_2 \in \mathbf{C}_0, \exists i \in \{1, 2, \dots, N_R\}, \text{s.t. } \sin \theta_i \geq \frac{\rho_{\text{ISAR}_i}}{\rho_{\text{rec}}}. \quad (26)$$

If the reconstruction resolution is larger than the resolution of ISAR images, (26) could be satisfied by adjusting the distribution of radars in the radar network. So, it is feasible to reconstruct the 3-D scattering image via radar network.

The analysis of the conditions is summarized in Table I. However, the specific reconstruction algorithm has not been considered in the abovementioned analysis, the condition related to the reconstruction algorithm is given in Section IV.

IV. 3-D SCATTERING IMAGE SPARSE RECONSTRUCTION

A. Data Representation and Mapping Process

At first, the appropriate data representation should be determined to reconstruct the positions and coefficients of the scattering points.

To contain all the scattering centers on the target, space is divided into N_x , N_y , and N_z grids along with the directions of the axes X , Y , and Z , respectively. Generally, the points in the space are regarded as a 3-D matrix, in which the values and the indexes represent the positions and scattering coefficients, respectively. However, another representation of the points is the index image, which contains the positions and scattering coefficients directly. As shown in Fig. 4, any general image can be transformed into an index image. To reconstruct the scattering coefficient and position simultaneously, the index image is more appropriate than the general image.

So, the matrix of spatial points can be expressed as

$$X = [\sigma \quad P]^T \quad (27)$$

where $P = [\overrightarrow{OP_1}, \overrightarrow{OP_2}, \dots, \overrightarrow{OP_N}]^T$ is the position vector of spatial points, $N = N_x N_y N_z$ is the spatial point number, and $\sigma = [\sigma_1, \sigma_2, \dots, \sigma_N]^T$ is the vector constituted by the scattering coefficients and zeros. Then, the mapping process for spatial points to an imaging plane should be described based on the data representation in (27).

Suppose that $\mathbf{u}_{u,i}$ and $\mathbf{u}_{w,i}$ are the unit vectors of axis U_i and W_i , as shown in Fig. 2, the point P is projected at the point Q_i on the imaging plane for radar- i . The coordinate of P is (x, y, z) in (O, X, Y, Z) and the coordinate of Q_i is (u, w) in (O, U_i, W_i) . The projecting process from (O, X, Y, Z) to (O, U_i, W_i) can be expressed as

$$[u \quad w]^T = \Phi_i [x \quad y \quad z]^T \quad (28)$$

TABLE I
CONDITIONS OF DIFFERENT CASES

Case	Point number	Number of imaging planes	Projection conditions	Number of projected points	Inverse-projection conditions	Number of reconstructed points	Final conditions
1	1	1	Axiom-1	1	Axiom-2 $\mathbf{n}_i \cap \mathbf{n}_j = \emptyset$	infinite	—
		2	Axiom-1	2	$\mathbf{n}_i \neq \mathbf{n}_j, \mathbf{n}_i \cap \mathbf{n}_j \neq \emptyset$	0	—
					$\mathbf{n}_i = \mathbf{n}_j$	infinite	—
2	2		$l_i < r_{ISAR_i}, l_j < r_{ISAR_j}$	2	Same to Case-1		—
			$l_i \geq r_{ISAR_i}$	3	(16)	2	(18)
			$l_i \geq r_{ISAR_i}, l_j \geq r_{ISAR_j}$	4	(16)	2	(17)
Any 2		2	$r_{rec} \times \sin q_i \geq r_{ISAR_i}$	3 or 4	(16)	2	(26)

where Φ_i is the projection matrix of the imaging plane for radar- i .

Since the projection vector $\overrightarrow{PQ_i}$ is perpendicular to the imaging plane, it should be perpendicular to $\mathbf{u}_{u,i}$ and $\mathbf{u}_{w,i}$. So, the relationship between points P and Q_i can be expressed as

$$\begin{cases} (\overrightarrow{OP} - \overrightarrow{OQ_i})^T \mathbf{u}_{u,i} = 0 \\ (\overrightarrow{OP} - \overrightarrow{OQ_i})^T \mathbf{u}_{w,i} = 0. \end{cases} \quad (29)$$

As the coordinate of Q_i is (u, w) in (O, U_i, W_i) , $\overrightarrow{OQ_i}$ can be expressed as $\overrightarrow{OQ_i} = u\mathbf{u}_{u,i} + w\mathbf{u}_{w,i}$. Equation (30) can be rewritten as

$$\begin{bmatrix} \mathbf{u}_{u,i} \\ \mathbf{u}_{w,i} \end{bmatrix} \left(\overrightarrow{OP} - [\mathbf{u}_{u,i}, \mathbf{u}_{w,i}] \begin{bmatrix} u \\ w \end{bmatrix} \right) = \mathbf{0}. \quad (30)$$

So, the coordinate of the projection point Q_i in (O, U_i, W_i) can be obtained by

$$\begin{bmatrix} u \\ w \end{bmatrix} = \left(\begin{bmatrix} \mathbf{u}_{u,i} \\ \mathbf{u}_{w,i} \end{bmatrix} [\mathbf{u}_{u,i}, \mathbf{u}_{w,i}] \right)^{-1} \begin{bmatrix} \mathbf{u}_{u,i} \\ \mathbf{u}_{w,i} \end{bmatrix} \overrightarrow{OP} = \Phi_i \overrightarrow{OP}. \quad (31)$$

According to (28), the spatial points are expressed as $X = [\sigma \ P]^T$ to contain the scattering coefficient and position. Φ_i in (31) is the projection matrix only for P . The projection matrix for X should be further expressed as

$$\Psi_i = \begin{bmatrix} \mathbf{1} \\ \Phi_i \end{bmatrix} \quad (32)$$

and the mapping process for the point P to point Q_i can be expressed as

$$[\sigma \ u \ w]^T = \Psi_i [\sigma \ x \ y \ z]^T. \quad (33)$$

Then, the mapping process for X can be expressed as

$$F_i(X) = \Psi_i X \quad (34)$$

where $F_i(\cdot)$ denotes the mapping process from the target to the imaging plane for the radar- i .

B. CS Reconstruction Model

It is an inverse problem to reconstruct the 3-D scattering image from the ISAR images of multiangles. To ensure the uniqueness of the solution, constraints should be added in the reconstruction problem.

Two issues should be minimized to establish the constraints of the reconstruction model: 1) reconstruction error and 2) sparsity of scattering centers.

To measure the reconstruction error, the sum of the differences between all the projection images and the ISAR images should be calculated. The index image of the ISAR image \mathbf{g}_i can be expressed as $\mathbf{G}_i = [\text{vec}(\mathbf{g}_i) \ \Phi_i \mathbf{P}]^T$, where $\text{vec}(\mathbf{g}_i)$ is the vectorization rearrangement of \mathbf{g}_i as the order of $\Phi_i \mathbf{P}$. Then, the constraint of reconstruction error can be expressed as

$$\sum_{i=1}^{N_R} \|F_i(X) - \mathbf{G}_i\|_2^2 \leq \eta_0 \quad (35)$$

where η_0 is a small threshold related to noise.

As all known, the scattering centers of aerospace targets are sparsely distributed in the space [1], [7]. If the element in \mathbf{P} is set to 0 when the element in σ is 0, \mathbf{P} and σ are the sparse vectors with the same support set. Then, X is a multiple measurement sparse vector. So, the 3-D scattering reconstruction model can be established as

$$\min J(X) \quad \text{s.t.} \quad \sum_{i=1}^{N_R} \|F_i(X) - \mathbf{G}_i\|_2^2 \leq \eta_0 \quad (36)$$

where $J(X)$ is the penalty function based on the sparsity prior of X . Since the sparse vector is a random variable in the noise environment, the form of penalty function is related to the prior probability distribution of the sparse vector. For example, the prior probability distribution of scattering centers obeys the Laplace of order p ($0 \leq p \leq 1$) in conventional SAR or ISAR imaging, and the penalty function can be expressed as $\|X\|_p^p$. However, the prior probability distribution of scattering centers in the 3-D space has not been studied. So, the penalty function can only be expressed as $L(X) = \|X\|_0$, which is the simplest form and it measures the number of scattering centers on the

target. Then, (36) can be rewritten as

$$\min \|X\|_0 \quad \text{s.t.} \quad \sum_{i=1}^{N_R} \|\Psi_i X - G_i\|_2^2 \leq \eta_0. \quad (37)$$

Utilizing the Lagrangian method, (37) can be expressed as

$$\hat{X} = \min_X \sum_{i=1}^{N_R} \|\Psi_i X - G_i\|_2^2 + \lambda \|X\|_0 \quad (38)$$

where λ is a constant related to the environment noise.

As the reconstruction model is given, the reconstruction condition can be further discussed. Suppose the number of imaging planes satisfying (25) is N_{plane} , (26) is the situation when $N_{\text{plane}} \geq 1$.

Suppose the correctly and the false reconstruction results are X and X' , respectively, the correct reconstruction result can be obtained only if the cost function of X is less than that of X' , which is expressed as

$$\sum_{i=1}^{N_R} \|\Psi_i X - G_i\|_2^2 + \lambda \|X\|_0 - \sum_{i=1}^{N_R} \|\Psi_i X' - G_i\|_2^2 - \lambda \|X'\|_0 < 0. \quad (39)$$

For any two scattering points P_1 and P_2 , suppose that X' only contains one of the two points and X contains both the two points, then $\|X'\|_0 = \|X\|_0 - 1$. If only the imaging plane for radar- j satisfies (25), the two points can only be distinguishable for the projection image on the j th imaging plane, and they are projected at one point on the other imaging planes. So, $\|\Psi_i X - G_i\|_2^2$ is equal to $\|\Psi_i X' - G_i\|_2^2$ only when $i \neq j$, and the cost function of X' can be expressed as

$$\begin{aligned} & \sum_{i=1}^{N_R} \|\Psi_i X' - G_i\|_2^2 + \lambda \|X'\|_0 \\ &= \sum_{i=1, i \neq j}^{N_R} \|\Psi_i X - G_i\|_2^2 + \|\Psi_j X' - G_i\|_2^2 + \lambda(\|X\|_0 - 1). \end{aligned} \quad (40)$$

Equation (40) can be further expressed as

$$\|\Psi_j X' - G_i\|_2^2 - \|\Psi_j X - G_i\|_2^2 > \lambda. \quad (41)$$

The following equation is suitable when $N_{\text{plane}} = 1$. As for the general situation, the condition can be extended as

$$\|\Psi_j X' - G_i\|_2^2 - \|\Psi_j X - G_i\|_2^2 > \frac{\lambda}{N_{\text{plane}}}, \quad 1 \leq N_{\text{plane}} \leq N_R. \quad (42)$$

Since λ is a constant, the larger N_{plane} is, the easier (42) can be satisfied. So, the more imaging planes satisfy (25), the better reconstruction result will be. And the best cases can be expressed as

$$\forall P_1, P_2 \in \mathbf{C}_0, \quad \forall i \in \{1, 2, \dots, N_R\}, \quad \text{s.t., } \sin \theta_i \geq \frac{\rho_{\text{ISAR}_i}}{\rho_{\text{rec}}}. \quad (43)$$

C. Dimensional Reduction by Layer Sparse

In the above sections, only the sparsity of the spatial points is considered. It causes the size of 3-D reconstruction to increase very rapidly with the increasing resolution of the ISAR images. To reduce the size of the 3-D scattering CS reconstruction problem, the deeper sparse structure should be analyzed. According to the geometry of the radar network, three kinds of point sets are defined: 1) the set of scattering points; 2) the set of feasible points; and 3) the set of spatial points.

First Layer: The set of scattering points is the minimal set to contain the whole scattering information of the target and it can be expressed as

$$\mathbf{C}^0 = \left\{ c_{n_0}^0 \mid c_{n_0}^0 = \left(\sigma_{n_0}^0, \overrightarrow{OP_{n_0}^0} \right), n_0 = 1, 2, \dots, N_0 \right\} \quad (44)$$

where $P_{n_0}^0$ denotes the n_0 th scattering point on the target, $\sigma_{n_0}^0$ is the scattering coefficient of n_0 th scattering point, and N_0 is the number of the scattering points.

The matrix representation of \mathbf{C}^0 can be written as

$$X^0 = [\sigma^0 \quad \mathbf{P}^0]^T \quad (45)$$

where $\sigma^0 = [\sigma_1^0, \sigma_2^0, \dots, \sigma_{N_0}^0]^T$ and $\mathbf{P}^0 = [\overrightarrow{OP_1^0}, \overrightarrow{OP_2^0}, \dots, \overrightarrow{OP_{N_0}^0}]^T$ are the vectors constituted by the scattering coefficients and the scattering position, respectively. Since $\sigma_{n_0}^0$ and $\overrightarrow{OP_{n_0}^0}$ are completely unknown, X^0 cannot be solved directly.

Second Layer: The set of feasible points is constituted by the points on the projection lines. It contains all the possible locations of the scattering points and can be expressed as

$$\begin{aligned} \mathbf{C}^1 &= \left\{ c_{n_1}^1 \mid c_{n_1}^1 = \left(\sigma_{n_1}^1, \overrightarrow{OP_{n_1}^1} \right), n_1 = 1, 2, \dots, N_1 \right\} \\ \text{s.t. } \sigma_{n_1}^1 &= \begin{cases} \sigma_{n_0}^0, & P_{n_1}^1 = P_{n_0}^0 \\ 0, & \text{else,} \end{cases} \quad \overrightarrow{OP_{n_1}^1} = \begin{cases} \overrightarrow{OP_{n_0}^0}, & P_{n_1}^1 = P_{n_0}^0 \\ 0, & \text{else} \end{cases} \end{aligned} \quad (46)$$

where $P_{n_1}^1$ denotes the n_1 th feasible point and $N_1 \gg N_0$.

The matrix representation of \mathbf{C}^1 can also be expressed as

$$X^1 = [\sigma^1 \quad \mathbf{P}^1]^T \quad (47)$$

where

$$\sigma^1 = [0, \dots, \sigma_{K_1}^1, \dots, \sigma_{K_{N_0}}^1, \dots, \sigma_{K_{N_0}}^1, \dots, 0]^T, \quad \sigma_{K_{N_0}}^1 = \sigma_{n_0}^0 \quad (48)$$

and

$$\begin{aligned} \mathbf{P}^1 &= [0, \dots, \overrightarrow{OP_{K_1}^1}, \dots, \overrightarrow{OP_{K_{N_0}}^1}, \dots, \overrightarrow{OP_{K_{N_0}}^1}, \dots, 0]^T \\ \overrightarrow{OP_{K_{N_0}}^1} &= \overrightarrow{OP_{n_0}^0} \end{aligned} \quad (49)$$

are sparse vectors with the same support set $\{K_1, K_2, \dots, K_{N_0}\}$. So, X^1 is a multiple measurement vector.

The feasible points can be determined before reconstruction processing. The difference image between the ISAR image and

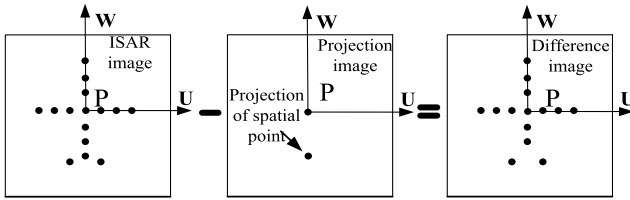


Fig. 5. Difference image between the ISAR image and the projection of a spatial point.

TABLE II
SIZE OF DIFFERENT LAYERS

First layer	N_0
Second layer	$N_R N_0 \min(N_x, N_y, N_z) \leq N_1 \leq N_R N_0 \ N_x, N_y, N_z\ _2$
Third layer	$N_x N_y N_z$

the projection for each point is shown in Fig. 5. For any point and any radar in the radar network, if the point coefficient is less than the value of its projected point on the ISAR image, the point belongs to the set of feasible points. Since the point coefficient is unknown before reconstruction processing, a point is feasible only if the value of its projected point is larger than a threshold α . Moreover, the union of the feasible points obtained by all radars in the network is the entire set of feasible points. The detailed procedure to find the feasible points is shown in Algorithm 1. Since the elements of \mathbf{P}^1 and the size N_1 can be obtained by finding the feasible points, X^1 is a sparse representation of X^0 and X^0 can be obtained from the reconstruction of X^1 .

Third Layer: The set of spatial points contains all the points in the 3-D space and it can be expressed as

$$\begin{aligned} \mathcal{C} = & \left\{ c_n \mid c_n = (\sigma_n, \overrightarrow{OP_n}), n=1, 2, \dots, N, N = N_x N_y N_z \right\} \\ \text{s.t. } \sigma_n = & \begin{cases} \sigma_{n_0}^0, & P_n = P_{n_0}^0 \\ 0, & \text{else,} \end{cases} \quad \overrightarrow{OP_n} = \begin{cases} \overrightarrow{OP_{n_0}^0}, & P_n = P_{n_0}^0 \\ 0, & \text{else.} \end{cases} \quad (50) \end{aligned}$$

The matrix representation of spatial points can be written as (28). Since the positions of the spatial points are known, $\overrightarrow{OP_n}$ can be calculated and the size is $N = N_x N_y N_z$. Then, X^0 can be sparse mapping in X , which means that X is a sparse representation containing all the information of X^0 . So, X^0 can be obtained from the reconstruction of X .

The layer sparse structure in radar network 3-D reconstruction is formed by the three kinds of sets, and the relationship between them is $\mathcal{C}^0 \subset \mathcal{C}^1 \subset \mathcal{C}$. The sizes of the different layers are shown in Table II.

According to the definition of the feasible points, the rough range of the feasible point number can be given. When the grids in the 3-D space are fixed, the projection lines are no longer than $\|(N_x, N_y, N_z)\|_2$ and no less than $\min(N_x, N_y, N_z)$. As a result, the column number of X and X^1 is $N = N_x N_y N_z$ and $N_R N_0 \min(N_x, N_y, N_z) \leq N_1 \leq N_R N_0 \|N_x, N_y, N_z\|_2$, respectively. In the radar network 3-D scattering reconstruction, the radar number N_R and the scattering point number N_0 are fixed. Compared with X , the size of X^1 has a linear increase rate with the resolution of the ISAR

Algorithm 1 3D Scattering Sparse Reconstruction via Radar Network

Input: Positions of the available radars; Velocity of the target; Position of the target center; Echo from each radar in the radar network;

Step 1) ISAR imaging for the echo received by each radar:

Obtain $\{\mathbf{g}_1, \mathbf{g}_2, \dots, \mathbf{g}_{N_R}\}$ by RD algorithm.

Step 2) Ensure the feasible points

Initialization: the feasible point set $\mathcal{C}^1 = \emptyset$.

for each radar $i \in [1, N_R]$ **do**

Initialization: $\beta_i = \emptyset$ and $\sigma = \mathbf{0}$;

for each spatial point $x \in [1, N_x], y \in [1, N_y], z \in [1, N_z]$

do

Calculate $[u \ w]^T = \Phi_i [x \ y \ z]^T$;

if $\mathbf{g}_i(uN_a' + w) \geq \alpha$,

Update $\beta_i = \beta_i \cup \{(\mathbf{g}_i(uN_a' + w), x, y, z)^T\}$;

end for

Update $\mathcal{C}^1 = \mathcal{C}^1 \cup \beta_i$

end for

Step 3) Solve the reconstruction model

Initialization: the matrix $X^1 = \mathbf{0}$, the residue error matrix

$\mathbf{R} = \mathbf{\Gamma}$ and the support set $\Omega = \emptyset$;

for $j = 1 : \min(N_0, |\mathcal{C}^1|)$

Calculate all the 1-norms for the lines in $\mathbf{H}^T \mathbf{R}$;

Find out the line index n_j for the maximum 1-norm;

Update the support set: $\Omega = \Omega \cup \{n_j\}$;

Update the solution matrix: $X^1(\Omega, :) = \mathbf{H}(:, \Omega)^\dagger \mathbf{R}$

Update the residue matrix: $\mathbf{R} = \mathbf{\Gamma} - \mathbf{H} X^1$

end for

Output: 3D scattering matrix X^1

images. So, the reconstruction model with lower size can be established as

$$\hat{X}^1 = \min_{X^1} \sum_{i=1}^{N_R} \|\Psi_i X^1 - \mathbf{G}_i^1\|_2^2 + \lambda \|X^1\|_0 \quad (51)$$

where $\mathbf{G}_i^1 = [\text{vec}(\mathbf{g}_i) \ \Phi_i \mathbf{P}^1]^T$.

To solve the above problem, we transform (51) to a standard CS model, and the constraint of reconstruction error in (51) should be further expressed as

$$\begin{aligned} \sum_{i=1}^{N_R} \|\Psi_i X^1 - \mathbf{G}_i^1\|_2^2 &= \sum_{i=1}^{N_R} \text{tr} \left\{ (\Psi_i X^1 - \mathbf{G}_i^1)^T (\Psi_i X^1 - \mathbf{G}_i^1) \right\} \\ &= \text{tr} \left\{ \sum_{i=1}^{N_R} (\Psi_i X^1 - \mathbf{G}_i^1)^T (\Psi_i X^1 - \mathbf{G}_i^1) \right\} \\ &= \text{tr} \left\{ (\mathbf{H} X^1 - \mathbf{\Gamma})^T (\mathbf{H} X^1 - \mathbf{\Gamma}) \right\} \\ &= \|\mathbf{H} X^1 - \mathbf{\Gamma}\|_2^2 \end{aligned} \quad (52)$$

where $\mathbf{H} = [\Psi_1^T, \Psi_2^T, \dots, \Psi_{N_R}^T]^T$ and $\mathbf{\Gamma} = [\mathbf{G}_1^{1, T}, \mathbf{G}_2^{1, T}, \dots, \mathbf{G}_{N_R}^{1, T}]^T$. Then, the standard CS model of radar network 3-D scattering reconstruction can be expressed as

$$\min \|X^1\|_0 \quad \text{s.t. } \|\mathbf{H} X^1 - \mathbf{\Gamma}\|_2^2 \leq \eta_0. \quad (53)$$

Rather than reconstruct X^0 from X directly, (53) utilizes the sparse structure with three layers to reconstruct X^0 from X^1 . Since X^1 is a multiple measurement vector, the multiple measurement vector orthogonal matching pursuit (MMV-OMP) algorithm [29] is chosen to solve the model in this article.

D. 3-D Scattering Reconstruction

The algorithm can be divided into three steps. In step 1), the ISAR images for all the radar are obtained by the RD algorithm.

In step 2), a search algorithm is designed to find the feasible points from the spatial points. The feasible point set for all the radars is initialized to $C^1 = \emptyset$. For each radar, the feasible point set and the coefficient vector of the spatial points are initialized to $\beta_i = \emptyset, i \in [1, N_R]$ and $\sigma = \mathbf{0}$, respectively. For each spatial point with the coordinate (x, y, z) , where $x \in [1, N_x], y \in [1, N_y], z \in [1, N_z]$, the coordinate of the projected point on the ISAR image can be calculated by $[u \ w]^T = \Phi_i [x \ y \ z]^T$. If the value of the projected point is larger than the threshold α , the spatial point is added into β_i . Then, the entire set of feasible points is updated by $C^1 = C^1 \cup \beta_i$.

In step 3), the CS model is solved by the MMV-OMP algorithm. Here is a brief introduction to the MMV-OMP algorithm and the detailed procedure is shown in [34]. The support set Ω , the solution matrix X^1 , and the residue error matrix R should be initialized before the iterations and be updated in each iteration. The 1-norms of the lines in the inner product matrix $H^T R$ are calculated, and the line index for the maximum 1-norm is added into the support set Ω . Then, the solution matrix is updated by $X^1(\Omega, :) = H(:, \Omega)^{\dagger} R$, where $X^1(\Omega, :)$ is the matrix formed by the lines of X^1 with the index of Ω , $H(:, \Omega)$ is the matrix formed by the columns of H with the index of Ω , and \dagger denotes the pseudo-inverse operator. The residue error matrix is updated by $R = \Gamma - H X^1$. Generally, a fixed iterative number or a threshold for the norm of the residue error matrix R can be chosen as the stopping criteria for the OMP algorithm. Since the feasible point number is obtained by step 2), the upper bound of the scattering point number N_0 can be given as $N_0 \leq N_1/N_R \min(N_x, N_y, N_z)$ according to the analysis for layer sparse. So, the iterative number $\min(N_0, N_1/N_R \min(N_x, N_y, N_z))$ is chosen for the stopping criteria. If the scattering point number N_0 is known, the iterative number is N_0 . If the scattering point number N_0 is unknown in some real cases, the iterative number is $N_1/N_R \min(N_x, N_y, N_z)$. As a result, the proposed method can work when the scatterer number is unknown, which is an improvement from PRN to our proposed method.

V. SIMULATIONS AND EXPERIMENTS

To verify the validity of the proposed method, both simulations and experiments are performed.

A. Simulations

The simulations are implemented with MATLAB v9.20.0 environment on a PC with a 3.6-GHz Intel i7 CPU. In the simulation, the radar network is made up of three imaging

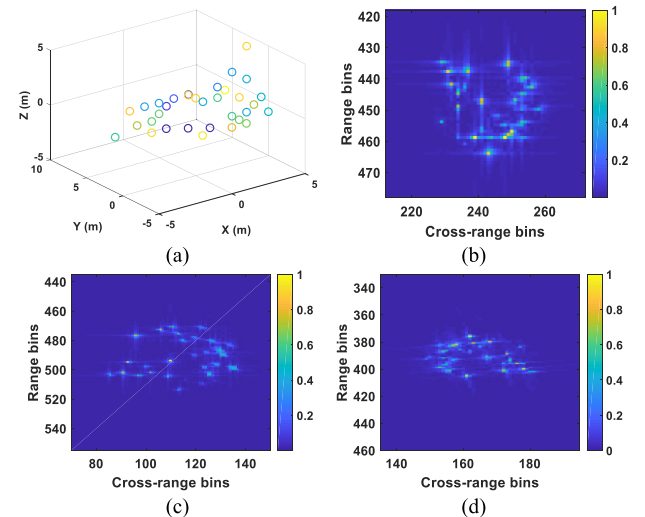


Fig. 6. Target model and 2-D ISAR images obtained by RD algorithm when SNR is -5 dB. (a) Target model. (b)–(d) ISAR images observed by radar-1 to radar-3, respectively.

TABLE III
SIMULATION PARAMETERS

parameter	value
Target Velocity V	(-450.35, -50.5, 0) m/s
Target Coordinates in imaging midpoint (x_0, y_0, z_0)	(0, 0, 0) m
Coordinates of Radar 1	(-11000, -10000, 750) m
Coordinates of Radar 2	(11000, -10000, 740) m
Coordinates of Radar 3	(0, 1730, 740) m
Signal-to-noise ratio (SNR)	-5 dB
Center frequency f_c	10 GHz
Pulse repetition frequency	1000Hz
Range resolution	0.3 m
Cross-range resolution	0.3 m
Space grid interval	0.4 m
Threshold α	0.2

radars, the target model is formed by 33 ideal scattering points, and the scattering coefficients are randomly generated, which is shown in Fig. 6(a). Assume the target parameters can be provided by the target tracking method. Suppose the radars transmit linear-frequency-modulated (LFM) signals. The simulation parameters are illustrated in Table III. The space grid interval is set as 0.4 m, and the target is assumed in a cube with a side length of 20 m. The target size d is 20 m, and the range L is not less than 1881.62 m. According to $\Delta d \leq L^2/2d$, the far-field error Δd is not more than 0.21 m. As a result, the far-field error is less than the space grid interval, and the far-field condition is satisfied.

In Fig. 6(b)–(d), the 2-D ISAR images observed by radar 1 to radar 3 are obtained by RD algorithm when SNR is -5 dB.

Utilizing the 2-D ISAR images observed from different angles in Fig. 6, radar network 3-D reconstruction results

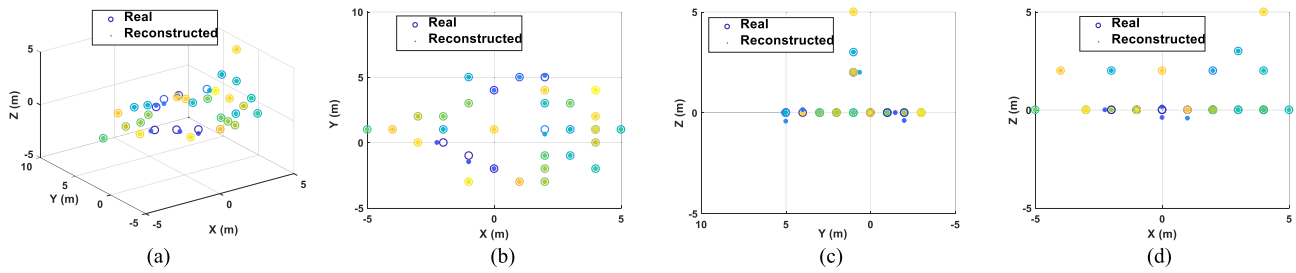


Fig. 7. Reconstructed results of CSRN using an aircraft model consisted of ideal point scattering centers. (a) 3-D reconstruction result. The real positions and the reconstructed results are denoted by the colored circles and the colored solid circles, respectively. The scattering coefficients are denoted by different colors. (b)–(d) Three views of (a).

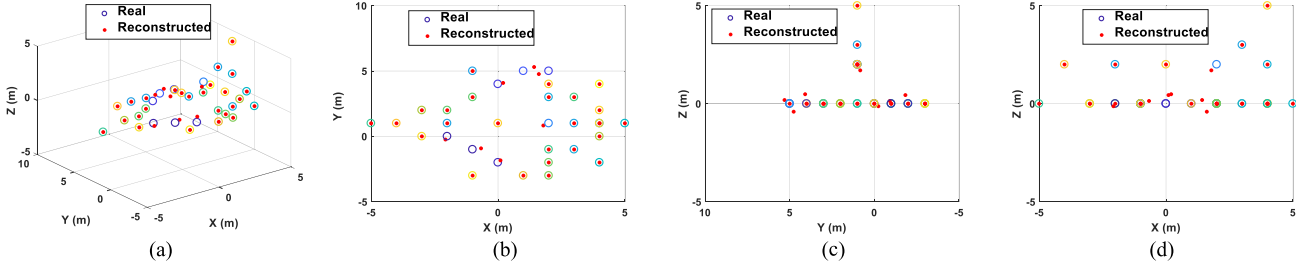


Fig. 8. Reconstructed results of PRN using an aircraft model consisted of ideal point scattering centers. (a) 3-D reconstruction result. (b)–(d) Three views of (a).

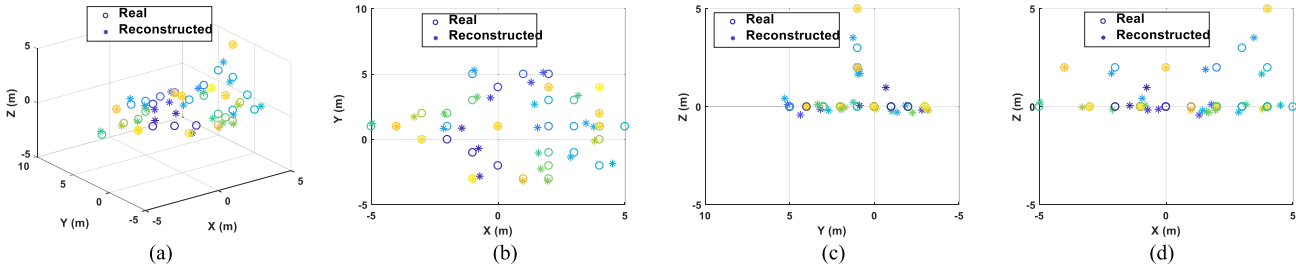


Fig. 9. Reconstructed results of InISAR 3-D imaging based on L-shaped antennas. (a) 3-D reconstruction result. (b)–(d) Three views of (a).

can be obtained. To make it fair, the iteration number of MMV-OMP is known as $N_0 = 33$ in CSRN since the scatterer number is required for PRN [27], [28]. The reconstructed results of the CSRN and the PRN are shown in Figs. 7 and 8, respectively. With the assumption that the scatterers in Fig. 6(b) and (c) are correctly associated, the imaging results of the InISAR technique [20], which utilize L-shaped three antennas and length of the baseline is 2 m, with the same target model and imaging parameters are shown in Fig. 9. As we can see, the information of the scattering coefficient is lost in Fig. 8 due to the binarized assumption of the PRN. However, the reconstructed scattering coefficients match quite well with the target model by the CSRN, and the error mainly exists in the reconstruction of the weak scattering centers. The proposed method gets better reconstruction performance than InISAR when SNR is -5 dB.

To test the antinoise performance of the proposed method, the variation of the RMSE for scattering position via 100 Monte Carlo trials is given in Fig. 10. When SNR is less than 10 dB, the RMSE of CSRN and PRN is less than that of InISAR, which is because the phase is more sensitive to the

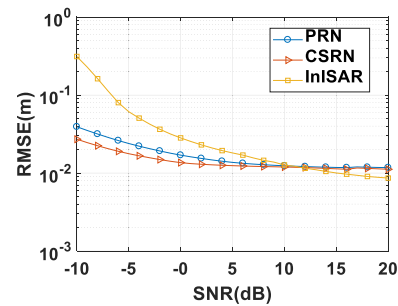


Fig. 10. Variation of the RMSE for scattering position with SNR.

noise than the amplitude. When SNR is over 10 dB, the RMSE of CSRN and PRN is larger than that of InISAR. Since the InISAR is based on coherent processing and the proposed method is based on noncoherent processing, the proposed method has a better performance in the low SNR environment but has worse performance in the high SNR environment.

Moreover, PRN, CSRN, and InISAR averagely take about 13.74, 1.436, and 0.0865 s in the above simulations, respectively. InISAR has the shortest running time because the

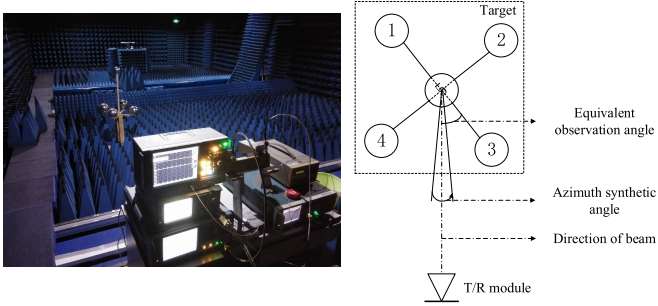


Fig. 11. Optical photograph and the top-view diagram of the experimental system 1.

interferometric processing is not an iterative optimization and the scatterers are assumed associated correctly. CSRN has shorter running time than PRN because the CSRN reconstructs the scatterers from the feasible points but PRN reconstructs the scatterers from the spatial points.

B. Experiments

To validate the proposed method further, the principle prototype experiment and the scaling experiment on real data have been performed. In the experiments, the scatterer number is unknown so that the PRN ceases to be effective. Only the proposed method can work for the experiments since the upper bound of the scatterer number can be obtained before reconstruction.

In the part of the principle prototype experiment, the target and the diagram of the experimental system are shown in Fig. 11. The target is constituted by five metal balls and it can rotate around the vertical axis. As the target is observed at several rotation angles, respectively, it is equal to the observation from a radar network. For the transmitted LFM continuous wave (LFMCW) signal, the carrier frequency is 14 GHz, the bandwidth is 6 GHz, and the pulse duration is 4 ms. In each observation angle, the azimuth synthetic angle is 14.4° and the cross-range sampling number is 400. The 2-D ISAR imaging results observed from 30° , 150° , 270° , 47° , 132° , and 198° are shown in Fig. 12(a)–(f), respectively. The first three equivalent observation angles are uniformly distributed, and the last three equivalent observation angles are randomly generated. The threshold α is 0.3. The range resolution and cross-range resolution of the ISAR images are 0.025 and 0.04 m, respectively. The target size d is 0.5 m and the range L is 10 m. According to $\Delta d \leq L^2/2d$, the far-field error Δd is not more than 0.0125 m. As a result, the far-field error is less than the resolution of the ISAR images, and the far-field condition is satisfied.

The comparison of 3-D reconstruction results of the uniform angles and the random angles is shown in Fig. 13. It is shown that the scattering distribution of the target is reconstructed successfully by the proposed method, and the 3-D scattering structure of the five metal balls is identifiable. Moreover, the experiment results show that the uniform angles perform better on the reconstruction effect than the random angles.

To avoid the occlusion problem, the minimum angle between different radars should be studied. The minimum angle can be calculated from the 3-D reconstruction conditions

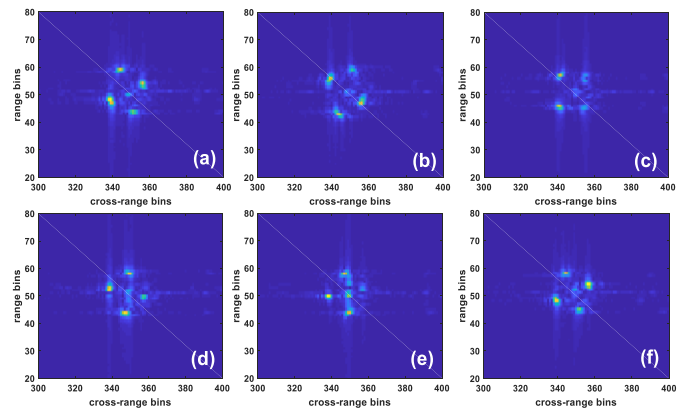


Fig. 12. 2-D ISAR imaging results of the five balls from different angles. (a)–(f) Observed from 30° , 150° , 270° , 47° , 132° , and 198° , respectively.

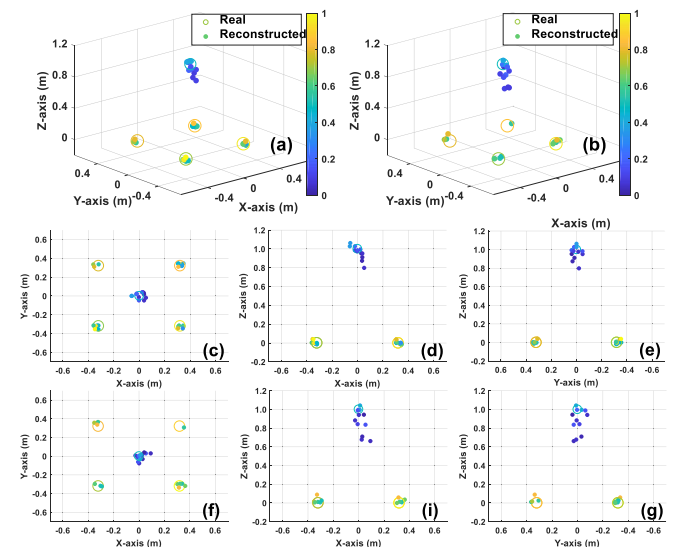


Fig. 13. Comparison of 3-D reconstruction results of the uniform angles and the random angles. (a) 3-D reconstruction results of the uniform angles. (b) 3-D reconstruction results of the random angles. (c)–(e) Three views of (a). (f), (g), and (i) Three views of (b).

in (26). The geometry of (26) can be expressed in Fig. 14. In Fig. 14, we move the normal vectors \mathbf{n}_i and \mathbf{n}_j to start from the point P_1 . As ρ_{ISAR_i} and ρ_{rec} are known, the cone around \mathbf{n}_i is determined. If (26) does not hold with the i th imaging plane, $\overrightarrow{P_1 P_2}$ is in the cone around \mathbf{n}_i . However, according to (26), we only need to require that $\overrightarrow{P_1 P_2}$ is not contained in one of the two cones around \mathbf{n}_i and \mathbf{n}_j . In Fig. 14, θ_{i-j} is the angle between the i th and j th imaging planes. If $\theta_{i-j} \geq \arcsin(\rho_{\text{ISAR}_i})/(\rho_{\text{rec}}) + \arcsin(\rho_{\text{ISAR}_j})/(\rho_{\text{rec}})$, $\overrightarrow{P_1 P_2}$ will be out of at least one cone, which means that (26) is satisfied. As a result, when the scattering points are undetermined, the minimum angle between any different two radars can be obtained by

$$\theta_{i-j} = \arcsin \frac{\rho_{\text{ISAR}_i}}{\rho_{\text{rec}}} + \arcsin \frac{\rho_{\text{ISAR}_j}}{\rho_{\text{rec}}}. \quad (54)$$

To verify the above conclusion, we traverse all the possible radar network distributions in the following experiment. As the target can rotate around the vertical axis, we chose the equivalent observation angles 0° , 5° , 10° , 15° , ..., 355°

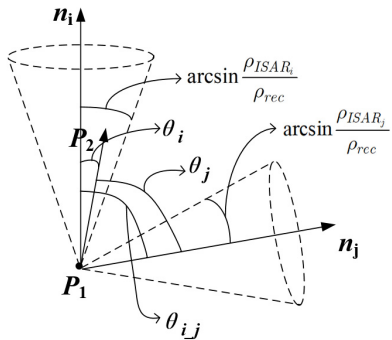
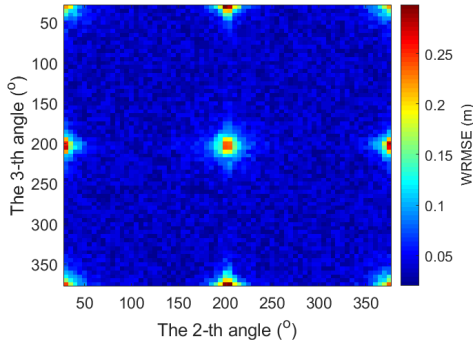


Fig. 14. Geometry of the reconstruction conditions.

Fig. 15. WRMSE for all the observed angles as the first observation angle is 0° .

to obtain 72 ISAR images. We observe the target from three angles. The first angle is fixed at 0° , and the other two angles are set from 5° to 355° . Then, all the possible distributions are traversed.

To evaluate the reconstruction performance, the weighted root mean squared error (WRMSE) $1/N_0 \sum_{n_0=1}^{N_0} \sigma_{n_0}^0 |r_{n_0}|^2$ is calculated, where N_0 is the number of the scatterers, $\sigma_{n_0}^0$ is the reconstructed coefficient of the n_0 th scattering point, and r_{n_0} is the distant reconstruction error of the n_0 th scattering point. For each distribution, the 3-D reconstruction result is generated and the WRMSE is calculated. Fig. 15 shows the WRMSE for all the observed angles. The symmetrical image of WRMSE is caused by the symmetry of the equivalent circle distribution for the radar network.

In this experiment, the range resolution of the ISAR image is 0.025 m, and the reconstruction resolution is set as 0.05 m. The minimum angle calculated from (54) is 60° . In Fig. 15, when the angle between different radars is larger than 60° , the WRMSE is less than 0.05 m. Since the reconstruction resolution is set as 0.05 m, the reconstruction result is mainly correct when the minimum angle between different radars is larger than 60° . The experimental result verifies the conclusion in (54).

In Fig. 15, the angle between different radars is 50° or 55° , which is less than the angle calculated by (54), and the WRMSE is also less than 0.1 m. Because the angle of (54) is obtained for any distribution of scattering points, the minimum angle may be less than (54) for a fixed distribution of scattering points. As a result, (54) is sufficient but nonessential condition for radar network 3-D reconstruction.

To validate the proposed method further, an all-metal scaling model experiment of F-16 in the microwave anechoic chamber has been performed. For the F-16 model, the intake and exhaust are filled with the radar absorbing materials, and the scaling factor is 1:8. The target model is observed independently of three different angles and the central angles are 0° , 45° , and 180° (0° is the head direction). In each observation, the azimuth synthetic angle is 5° and the sampling interval is 0.01° . The frequency range is from 34.2857 to 37.9428 GHz, and the number of frequency points is 701. The target is measured in the microwave anechoic chamber with the compact range. The signal generation and collection are implemented by an HP8510B vector network analyzer (VNA). The threshold α is 30. The range bins and cross-range bins of ISAR images are 0.004 m. The space grid interval is set to 0.005 m, and the target is assumed in a cube with a side length of 2 m.

In the 3-D scattering reconstruction, the grid interval is set to 0.05 m. As shown in Fig. 16(a)–(c), the 2-D ISAR images from 0° , 45° , and 180° are provided by the broadband sweep technique. The 3-D scattering reconstruction result of the proposed method is shown in Fig. 16(d)–(g), in which it can see the identifiable 3-D scattering structure of F-16. The reconstruction result can provide the 3-D scattering structure rather than a 2-D curved surface obtained by InISAR technique.

For the proposed method, the scatterers are matched by the way of image to image rather than the way of point to point. If the scatterer is strong in one ISAR image, and it is weak in another ISAR image, then the scatterer on the reconstruction image will be the compromise of both because the reconstruction error is the sum of the difference between the projection images and the ISAR images. As a result, not each scatterer can be matched very well by the proposed method. Considering the anisotropy scattering, in fact, the scatterers are difficult to be matched accurately. So, we chose to control the overall error to keep the reconstruction quality for the anisotropy scattering. For example, in Fig. 16(a)–(c), the white circle is for the same position on the target. Since attitudes observed from different radars are different, the scatters are weak in Fig. 16(a) but strong in Fig. 16(b) and (c). To minimize the reconstruction error, the reconstructed scatters in the white are the compromise of the three views, so we can see that the scatters in Fig. 16(h) are stronger than that in Fig. 16(a). For an opposite example, in Fig. 16(a)–(c), the red box is also for the same position on the target. Since attitudes observed from different radars are different, the scatters in Fig. 16(a) are lost in Fig. 16(b) and (c). To minimize the reconstruction error and the sparsity of scatters, the reconstructed scatters in the red box are abandoned, so we can see that the scatters in Fig. 16(j) are lost.

For the simple simulations, the 3-D target geometry may be able to be recovered by several methods. For the real target of the experiments, however, the PRN or InISAR ceases to be effective. Since the proposed CSRN avoids the scatterer association and it can reconstruct the scattering positions and

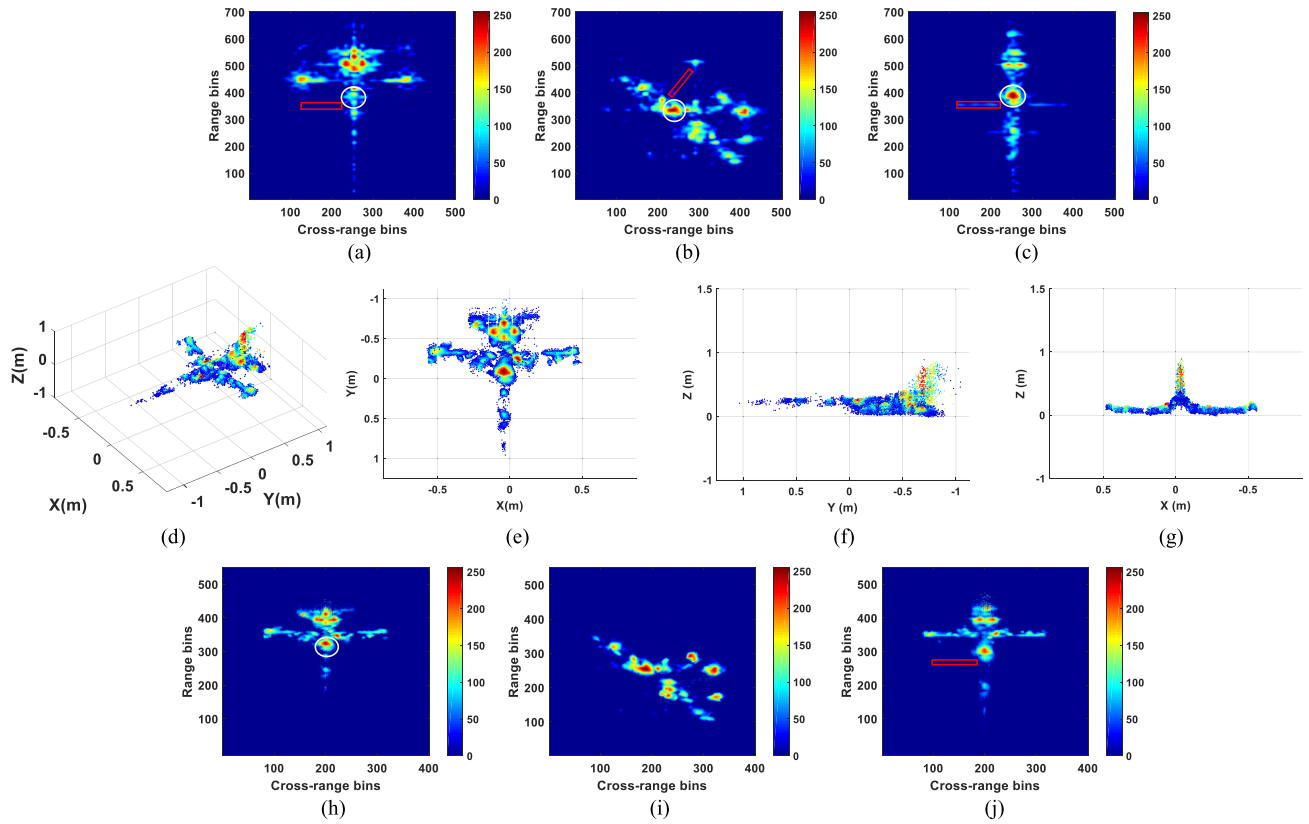


Fig. 16. Experimental results using an all-metal scaling model of F-16 in the microwave anechoic chamber. The head direction of F-16 is set to 0° . (a)–(c) ISAR images observed from 0° , 45° , and 180° , respectively. (d) 3-D scattering reconstruction result. (e), (f), and (g) Three views of (d). (h), (i), and (j) Projection images of the 3-D reconstruction result from 0° , 45° , and 180° .

scattering coefficients simultaneously, the proposed CSRN is effective for the complex real target.

VI. CONCLUSION

In this article, a novel 3-D scattering sparse reconstruction method is proposed based on the radar network. At first, the general signal model of radar network consisting of multiple independent imaging radars is given. Then, the projection relationship for mapping the points of targets on the imaging plane is derived briefly, and the reconstruction conditions of radar network 3-D reconstruction are given. To the end, the 3-D scattering distribution reconstruction mode is built in a CS framework, and a fast 3-D reconstruction algorithm is proposed. Compared with the existing 3-D reconstruction method based on the radar network, the proposed method can hold the information of the scattering coefficients by utilizing multiple ISAR images without binarization. To reduce the problem size, the layer sparse structure of radar network 3-D reconstruction is analyzed and the upper bound of the scatterer number can be predicted before reconstruction. Both the numerical simulations and the principle prototype experiments in the microwave anechoic chamber are shown to demonstrate the validity of the proposed method.

REFERENCES

- [1] V. C. Chen and M. Martorella, *Inverse Synthetic Aperture Radar Imaging: Principles, Algorithms and Applications*, vol. 1. Karachi, Pakistan: Shitech Publication, 2014.
- [2] D. A. Auscherman, A. Kozma, J. L. Walker, H. M. Jones, and E. C. Poggio, "Developments in radar imaging," *IEEE Trans. Aerosp. Electron. Syst.*, vol. AES-20, no. 1, pp. 363–400, Jan. 1984.
- [3] Y. Li, T. Su, J. Zheng, and X. He, "ISAR imaging of targets with complex motions based on modified Lv's distribution for cubic phase signal," *IEEE J. Sel. Topics Appl. Earth Observ. Remote Sens.*, vol. 8, no. 10, pp. 4775–4784, Oct. 2015.
- [4] M. Martorella, E. Giusti, A. Capria, F. Berizzi, and B. Bates, "Automatic target recognition by means of polarimetric ISAR images and neural networks," *IEEE Trans. Geosci. Remote Sens.*, vol. 47, no. 11, pp. 3786–3794, Nov. 2009.
- [5] Z. Zhu, Z. She, and J. Zhou, "Multiple moving target resolution and imaging based on ISAR principle," in *Proc. IEEE Nat. Aerosp. Electron. Conf. (NAECON)*, Jun. 1995, pp. 982–987.
- [6] K. K. Knaell and G. P. Cardillo, "Radar tomography for the generation of three-dimensional images," *IEE Proc.-Radar, Sonar Navigat.*, vol. 142, no. 2, pp. 54–60, Apr. 1995.
- [7] J. Yan, H. Liu, W. Pu, H. Liu, Z. Liu, and Z. Bao, "Joint threshold adjustment and power allocation for cognitive target tracking in asynchronous radar network," *IEEE Trans. Signal Process.*, vol. 65, no. 12, pp. 3094–3106, Jun. 2017.
- [8] J. Yan, W. Pu, S. Zhou, H. Liu, and Z. Bao, "Collaborative detection and power allocation framework for target tracking in multiple radar system," *Inf. Fusion*, vol. 55, pp. 173–183, Mar. 2020.
- [9] X.-W. Liu, Q. Zhang, Y.-C. Chen, L.-H. Su, and Y.-J. Chen, "Task allocation optimization for multi-target ISAR imaging in radar network," *IEEE Sensors J.*, vol. 18, no. 1, pp. 122–132, Jan. 2018.
- [10] Y. Wang and X. L. Li, "3D imaging based on combination of the ISAR technique and a MIMO radar system," *IEEE Trans. Geosci. Remote Sens.*, vol. 56, no. 10, pp. 6033–6054, Oct. 2018.
- [11] Q. Zhang and T. S. Yeo, "Three-dimensional SAR imaging of a ground moving target using the InSAR technique," *IEEE Trans. Geosci. Remote Sens.*, vol. 42, no. 9, pp. 1818–1828, Sep. 2004.
- [12] T. Cooke, "Ship 3D model estimation from an ISAR image sequence," in *Proc. Int. Radar Conf.*, Sep. 2003, pp. 36–41.

- [13] D.-W. Wang, X.-Y. Ma, A.-L. Chen, and Y. Su, "High-resolution imaging using a wideband MIMO radar system with two distributed arrays," *IEEE Trans. Image Process.*, vol. 19, no. 5, pp. 1280–1289, May 2010.
- [14] G. Q. Duan, D. W. Wang, X. Y. Ma, and Y. Su, "Three-dimensional imaging via wideband MIMO radar system," *IEEE Geosci. Remote Sens. Lett.*, vol. 7, no. 3, pp. 445–449, Jul. 2010.
- [15] F. Gu, F. Zhu, L. Chi, and Q. Zhang, "Single snapshot imaging method in multiple-input multiple-output radar with sparse antenna array," *IET Radar, Sonar Navigat.*, vol. 7, no. 5, pp. 535–543, Jun. 2013.
- [16] M. Soumekh, "Automatic aircraft landing using interferometric inverse synthetic aperture radar imaging," *IEEE Trans. Image Process.*, vol. 5, no. 9, pp. 1335–1345, Sep. 1996.
- [17] Y. Wang and X. F. Chen, "Three-dimensional geometry reconstruction of ship targets with complex motion for interferometric ISAR with sparse aperture," *J. Radars*, vol. 7, no. 3, pp. 320–334, Mar. 2018.
- [18] Y. Luo, Y.-J. Chen, Y.-Z. Zhu, W.-Y. Li, and Q. Zhang, "Doppler effect and micro-Doppler effect of vortex-electromagnetic-wave-based radar," *IET Radar, Sonar Navigat.*, vol. 14, no. 1, pp. 2–9, Jan. 2020, doi: 10.1049/iet-rsn.2019.0124.
- [19] X. Xu and R. M. Narayanan, "Three-dimensional interferometric ISAR imaging for target scattering diagnosis and modeling," *IEEE Trans. Image Process.*, vol. 10, no. 7, pp. 1094–1102, Jul. 2001.
- [20] Y. Sun, Y. Luo, Q. Zhang, J. Hu, and W. Huo, "Time-varying three-dimensional interferometric imaging for space rotating targets with stepped-frequency chirp signal," *IET Radar, Sonar Navigat.*, vol. 11, no. 9, pp. 1397–1405, Sep. 2017.
- [21] B. Tian, J. Zou, Z. Chen, and S. Xu, "Squint model interferometric ISAR imaging based on respective reference range selection and squint iteration improvement," *IET Radar, Sonar Navigat.*, vol. 9, no. 9, pp. 1366–1375, Dec. 2015.
- [22] Y. Wang and X. Chen, "3-D InISAR imaging of the ship target based on joint cross S-method algorithm," *IEEE Geosci. Remote Sens. Lett.*, vol. 16, no. 7, pp. 1080–1084, Jul. 2019.
- [23] M. Iwamoto and T. Kirimoto, "A novel algorithm for reconstructing three dimensional target shapes using sequential radar images," in *Proc. IEEE IGARSS*, vol. 4, Jul. 2001, pp. 1607–1609.
- [24] K. Suwa, K. Yamamoto, M. Iwamoto, and T. Kirimoto, "Reconstruction of 3D target geometry using radar movie," in *Proc. EUSAR*, 2008, pp. 149–152.
- [25] Y. Hui and X. Bai, "RID image series-based high-resolution three-dimensional imaging of micromotion targets," *J. Radars*, vol. 7, no. 5, pp. 548–556, Oct. 2018.
- [26] K. Suwa, T. Wakayama, and M. Iwamoto, "Three-dimensional target geometry and target motion estimation method using multistatic ISAR movies and its performance," *IEEE Trans. Geosci. Remote Sens.*, vol. 49, no. 6, pp. 2361–2373, Jun. 2011.
- [27] X.-W. Liu, Q. Zhang, S.-Q. Liu, Y.-C. Chen, and L. Sun, "A 3D image reconstruction technique for spinning targets based on radar networks," *Remote Sens. Lett.*, vol. 10, no. 2, pp. 158–167, Feb. 2019.
- [28] X.-W. Liu, Q. Zhang, L. Jiang, J. Liang, and Y.-J. Chen, "Reconstruction of three-dimensional images based on estimation of spinning target parameters in radar network," *Remote Sens.*, vol. 10, no. 12, p. 1997, Dec. 2018.
- [29] J. A. Tropp, A. C. Gilbert, and M. J. Strauss, "Algorithms for simultaneous sparse approximation. Part I: Greedy pursuit," *Signal Process.*, vol. 86, no. 3, pp. 572–588, Mar. 2006.



Ying Luo (Member, IEEE) was born in Hunan, China, in 1984. He received the M.S. degree in electrical engineering from the Institute of Telecommunication Engineering, Air Force Engineering University (AFEU), Xi'an, China, in 2008, and the Ph.D. degree in electrical engineering from AFEU, in 2013.

He was a Post-Doctoral Fellow with the National Laboratory of Radar Signal Processing, Xidian University, Xi'an, from 2014 to 2017, and a Visiting Scholar with the Department of Electrical and Computer Engineering, National University of Singapore, Singapore, from 2017 to 2018. He is an Associated Professor or a Ph.D. Advisor with the Institute of Information and Navigation, AFEU. He is also an Adjunct Associated Professor with the Key Laboratory for Information Science of Electromagnetic Waves, Ministry of Education, Fudan University, Shanghai, China. He has authored over 3 books and 100 articles on journals and conferences. Two of these articles won the First-Grade Prize of Shaanxi Natural Science Excellent Academic Paper in 2010 and 2013, respectively. His research interests include signal processing and autotarget recognition (ATR) in SAR and inverse synthetic aperture radar (ISAR).



Kun Zhang (Senior Member, IEEE) received the M.S. degree in mathematics from Shaanxi Normal University, Xi'an, China, in 1988, and the Ph.D. degree in electrical engineering from Xidian University, Xi'an, in 2001.

He was a Research Engineer from 2001 to 2003 and a Research Fellow from 2005 to 2006 with the Department of Electrical and Computer Engineering, National University of Singapore, Singapore. He is a Professor with the Institute of Information and Navigation, Air Force Engineering University, Xi'an, and an Adjunct Professor with the Key Laboratory for Information Science of Electromagnetic Waves, Ministry of Education, Fudan University, Shanghai, China. He has authored over 200 articles on journals and conferences. His main research interests include signal processing, clutter suppression, and its application in SAR and inverse synthetic aperture radar (ISAR).



Xiao-Wen Liu was born in Shaanxi, China, in 1991. He received the M.S. and Ph.D. degrees in electrical engineering from the Institute of Information and Navigation, Air Force Engineering University (AFEU), Xi'an, China, in 2015 and 2019, respectively.

He is with the School of Information and Communications, National University of Defense Technology, Xi'an. He has authored over 20 articles on journals and conferences. His research interests include radar signal processing and intelligence algorithm.



Bi-Shuai Liang received the Ph.D. degree in electrical engineering from Air Force Engineering University (AFEU), Xi'an, China, in 2014.

He is a Post-Doctoral Fellow with the Institute of Information and Navigation, AFEU. His research interests include radar signal processing and experimental design.



Le Kang was born in Shaanxi, China, in 1993. He received the B.S. degree from Tsinghua University, Beijing, China, in 2015, and the M.S. degree in electrical engineering from the Institute of Information and Navigation, Air Force Engineering University (AFEU), Xi'an, China, in 2017, where he is pursuing the Ph.D. degree.

His research interests include signal processing and autotarget recognition (ATR) in SAR and inverse synthetic aperture radar (ISAR).